

## Performance of the neutron time-of-flight facility n\_TOF at CERN

C. Guerrero<sup>1,a</sup>, A. Tsinganis<sup>1,2</sup>, E. Berthoumieux<sup>3,1</sup>, M. Barbagallo<sup>4</sup>, F. Belloni<sup>3</sup>, F. Gunsing<sup>3</sup>, C. Weiß<sup>5,1</sup>, E. Chiaveri<sup>3,1</sup>, M. Calviani<sup>1</sup>, V. Vlachoudis<sup>1</sup>, S. Altstadt<sup>6</sup>, S. Andriamonje<sup>1</sup>, J. Andrzejewski<sup>7</sup>, L. Audouin<sup>8</sup>, V. Bécares<sup>9</sup>, F. Bečvář<sup>10</sup>, J. Billowes<sup>11</sup>, V. Boccone<sup>1</sup>, D. Bosnar<sup>12</sup>, M. Brugger<sup>1</sup>, F. Calviño<sup>13</sup>, D. Cano-Ott<sup>9</sup>, C. Carrapico<sup>14</sup>, F. Cerutti<sup>1</sup>, M. Chin<sup>1</sup>, N. Colonna<sup>4</sup>, G. Cortés<sup>13</sup>, M.A. Cortés-Giraldo<sup>15</sup>, M. Diakaki<sup>2</sup>, C. Domingo-Pardo<sup>16</sup>, I. Duran<sup>17</sup>, R. Dressler<sup>18</sup>, N. Dzysiuk<sup>19</sup>, C. Eleftheriadis<sup>20</sup>, A. Ferrari<sup>1</sup>, K. Fraval<sup>3</sup>, S. Ganesan<sup>21</sup>, A.R. García<sup>9</sup>, G. Giubrone<sup>16</sup>, K. Göbel<sup>6</sup>, M.B. Gómez-Hornillos<sup>13</sup>, I.F. Gonçalves<sup>14</sup>, E. González-Romero<sup>9</sup>, E. Griesmayer<sup>5</sup>, P. Gurusamy<sup>21</sup>, A. Hernández-Prieto<sup>1,13</sup>, P. Gurusamy<sup>21</sup>, D.G. Jenkins<sup>22</sup>, E. Jericha<sup>5</sup>, Y. Kadi<sup>1</sup>, F. Käppeler<sup>23</sup>, D. Karadimos<sup>2</sup>, N. Kivel<sup>18</sup>, P. Koehler<sup>24</sup>, M. Kokkoris<sup>2</sup>, M. Krtička<sup>10</sup>, J. Kroll<sup>10</sup>, C. Lampoudis<sup>3</sup>, C. Langer<sup>6</sup>, E. Leal-Cidoncha<sup>17</sup>, C. Lederer<sup>6,25</sup>, H. Leeb<sup>5</sup>, L.S. Leong<sup>8</sup>, R. Losito<sup>1</sup>, A. Manousos<sup>20</sup>, J. Marganiec<sup>7</sup>, T. Martínez<sup>9</sup>, C. Massimi<sup>26</sup>, P.F. Mastinu<sup>19</sup>, M. Mastromarco<sup>4</sup>, M. Meaze<sup>4</sup>, E. Mendoza<sup>9</sup>, A. Mengoni<sup>27</sup>, P.M. Milazzo<sup>28</sup>, F. Mingrone<sup>26</sup>, M. Mirea<sup>29</sup>, W. Mondalaers<sup>30</sup>, T. Papaevangelou<sup>3</sup>, C. Paradela<sup>17</sup>, A. Pavlik<sup>25</sup>, J. Perkowski<sup>7</sup>, A. Plompen<sup>30</sup>, J. Praena<sup>15</sup>, J.M. Quesada<sup>15</sup>, T. Rauscher<sup>31</sup>, R. Reifarh<sup>6</sup>, A. Riego<sup>13</sup>, F. Roman<sup>1,29</sup>, C. Rubbia<sup>1,32</sup>, M. Sabate-Gilarte<sup>15</sup>, R. Sarmiento<sup>14</sup>, A. Saxena<sup>21</sup>, P. Schillebeeckx<sup>30</sup>, S. Schmidt<sup>6</sup>, D. Schumann<sup>18</sup>, P. Steinegger<sup>18</sup>, G. Tagliente<sup>4</sup>, J.L. Tain<sup>16</sup>, D. Tarrío<sup>17</sup>, L. Tassan-Got<sup>8</sup>, S. Valenta<sup>10</sup>, G. Vannini<sup>26</sup>, V. Variale<sup>4</sup>, P. Vaz<sup>14</sup>, A. Ventura<sup>27</sup>, R. Versaci<sup>1</sup>, M.J. Vermeulen<sup>22</sup>, R. Vlastou<sup>2</sup>, A. Wallner<sup>25</sup>, T. Ware<sup>11</sup>, M. Weigand<sup>6</sup>, T. Wright<sup>11</sup>, and P. Žugec<sup>12</sup>

<sup>1</sup> European Organization for Nuclear Research (CERN), Geneva, Switzerland

<sup>2</sup> National Technical University of Athens (NTUA), Greece

<sup>3</sup> Commissariat à l'Énergie Atomique (CEA) Saclay - Irfu, Gif-sur-Yvette, France

<sup>4</sup> Istituto Nazionale di Fisica Nucleare, Bari, Italy

<sup>5</sup> Atominstitut, Technische Universität Wien, Austria

<sup>6</sup> Johann-Wolfgang-Goethe Universität, Frankfurt, Germany

<sup>7</sup> Uniwersytet Łódzki, Lodz, Poland

<sup>8</sup> Centre National de la Recherche Scientifique/IN2P3 - IPN, Orsay, France

<sup>9</sup> Centro de Investigaciones Energeticas Medioambientales y Tecnológicas (CIEMAT), Madrid, Spain

<sup>10</sup> Charles University, Prague, Czech Republic

<sup>11</sup> University of Manchester, Oxford Road, Manchester, UK

<sup>12</sup> Department of Physics, Faculty of Science, University of Zagreb, Croatia

<sup>13</sup> Universitat Politècnica de Catalunya, Barcelona, Spain

<sup>14</sup> Instituto Tecnológico e Nuclear, Instituto Superior Técnico, Universidade Técnica de Lisboa, Lisboa, Portugal

<sup>15</sup> Universidad de Sevilla, Spain

<sup>16</sup> Instituto de Física Corpuscular, CSIC - Universidad de Valencia, Spain

<sup>17</sup> Universidade de Santiago de Compostela, Spain

<sup>18</sup> Paul Scherrer Institut, Villigen PSI, Switzerland

<sup>19</sup> Istituto Nazionale di Fisica Nucleare, Laboratori Nazionali di Legnaro, Italy

<sup>20</sup> Aristotle University of Thessaloniki, Thessaloniki, Greece

<sup>21</sup> Bhabha Atomic Research Centre (BARC), Mumbai, India

<sup>22</sup> University of York, Heslington, York, UK

<sup>23</sup> Karlsruhe Institute of Technology, Campus Nord, Institut für Kernphysik, Karlsruhe, Germany

<sup>24</sup> Oak Ridge National Laboratory (ORNL), Oak Ridge, TN 37831, USA

<sup>25</sup> University of Vienna, Faculty of Physics, Austria

<sup>26</sup> Dipartimento di Fisica, Università di Bologna, and Sezione INFN di Bologna, Italy

<sup>27</sup> Agenzia nazionale per le nuove tecnologie, l'energia e lo sviluppo economico sostenibile (ENEA), Bologna, Italy

<sup>28</sup> Istituto Nazionale di Fisica Nucleare, Trieste, Italy

<sup>29</sup> Horia Hulubei National Institute of Physics and Nuclear Engineering - IFIN HH, Bucharest - Magurele, Romania

<sup>30</sup> European Commission JRC, Institute for Reference Materials and Measurements, Retieseweg 111, B-2440 Geel, Belgium

<sup>31</sup> Department of Physics and Astronomy - University of Basel, Basel, Switzerland

<sup>32</sup> Laboratori Nazionali del Gran Sasso dell'INFN, Assergi (AQ), Italy

Received: 23 November 2012 / Revised: 4 February 2013

Published online: 25 February 2013

© The Author(s) 2013. This article is published with open access at Springerlink.com

Communicated by D. Pierroutsakou

**Abstract.** The neutron time-of-flight facility n\_TOF features a white neutron source produced by spallation through 20 GeV/c protons impinging on a lead target. The facility, aiming primarily at the measurement of neutron-induced reaction cross sections, was operating at CERN between 2001 and 2004, and then underwent a major upgrade in 2008. This paper presents in detail all the characteristics of the new neutron beam in the currently available configurations, which correspond to two different collimation systems and two choices of neutron moderator. The characteristics discussed include the intensity and energy dependence of the neutron flux, the spatial profile of the beam, the in-beam background components and the energy resolution/broadening. The discussion of these features is based on dedicated measurements and Monte Carlo simulations, and includes estimations of the systematic uncertainties of the mentioned quantities.

## 1 Introduction and objectives

The accurate knowledge of a wide variety of nuclear data is essential for the understanding of many of the processes occurring in nature and also playing a key role in nuclear technologies. In particular, neutron-induced reactions are the driving force behind the nucleosynthesis of elements beyond iron in stars (via the *s*- and *r*-processes) [1], the functioning of present nuclear reactors [2, 3] as well as the future ones aiming at minimizing nuclear waste (Generation-IV) [4] or reducing it (ADS) [5], the damage caused in the structural material of future fusion reactors [6], etc. In all these fields, the cross sections of a large number of neutron-induced reactions are the main ingredient in the associated calculations.

The cross sections available in different nuclear libraries (for instance, JEFF, ENDF, JENDL [7] for nuclear technologies and KADoNiS [8] for astrophysics) are derived from evaluations based on both experimental data and theoretical predictions from nuclear models. Nevertheless, the cross sections given in different evaluations are frequently incompatible and their accuracy is lower than needed. This makes it necessary to perform new and more accurate measurements of many isotopes and reactions, which are summarized for instance by the Nuclear Energy Agency in its High Priority Request List [9], but also in review papers on data needs for fusion [10] and astrophysics [1].

The neutron energy ranges of interest span from thermal (25 meV) to hundreds of MeV, depending on the application. In such a wide energy range the neutron cross sections have resonant structures and abrupt reaction thresholds which change significantly from isotope to isotope and cannot be predicted, thus requiring high energy resolution measurements to resolve such structures. This is preferably done by using the *Time-of-Flight* (ToF) technique in which a pulsed neutron beam, spanning over a wide range of energies, travels a given distance before reaching the sample under study. In this technique the kinetic energy of the neutrons is determined from their time of arrival at the measuring station. The kinetic energy  $E_n$

of neutrons with a speed  $v = L/t$  can be expressed as

$$E_n = E - mc^2 = \sqrt{c^2 p^2 + m^2 c^4} - mc^2 = mc^2(\gamma - 1), \quad (1)$$

where  $\gamma = (1 - v^2/c^2)^{-1/2}$ , and  $c$  is the speed of light. The first term of the series expansion gives the classical expression for the neutron kinetic energy, which shall be used below a few MeV,

$$E_n = \frac{1}{2}mv^2 = \alpha^2 \frac{L^2}{t^2}. \quad (2)$$

Taking, for instance, the value of the speed of light  $c = 299.8 \text{ m}/\mu\text{s}$  and  $m = 939.6 \text{ MeV}/c^2$  for the neutron mass, one obtains  $\alpha = 72.29 \frac{\sqrt{eV}\mu\text{s}}{\text{m}}$ .

Regarding the relative energy resolution of a ToF facility, this is given to a first approximation (see sect. 6 for details) by

$$\frac{\Delta E_n}{E_n} = 2 \times \sqrt{\left(\frac{\Delta t}{t}\right)^2 + \left(\frac{\Delta L}{L}\right)^2}, \quad (3)$$

and therefore the capability for resolving the resonance structures in the cross sections is favored by the use of long flight paths (large  $L$  and  $t$ ) and the production of all neutrons within the shortest possible time ( $\Delta t$ ) and smallest possible space ( $\Delta L$ ).

At present there are several neutron ToF facilities in the world devoted to the measurement of neutron-induced reactions cross sections. These use different methods for neutron production and have flight path lengths ranging between less than one meter to 400 m. Among these, the most active in the recent years are (flight paths are given in parenthesis) the n\_TOF facility [11–14] (185 m) discussed further in this paper, GELINA at JRC-IRMM in Belgium [15] (10, 30, 50, 60, 100, 200, 300 and 400 m), DANCE at LANSCE in the USA [16] (20 m) and AN-NRI at J-PARK in Japan [17] (22 and 28 m). In addition, two new facilities will soon become operational in Europe: n\_TOF-EAR2 at CERN in Switzerland [18] (20 m) and FRANZ in Germany [19] (0.8 m).

<sup>a</sup> e-mail: carlos.guerrero@cern.ch

The n\_TOF facility became operational at CERN (Geneva, Switzerland) in 2001 and has since then become a major facility in the field of neutron cross section measurements. In addition, measurements aimed at the study of nuclear structure and the mechanism of fission reactions are part of the experimental program. The facility ran between 2001 and 2004 (n\_TOF-Phase1) and, after a four-year halt and a complete upgrade of the neutron production target, it resumed operation at the end of 2008 (start of n\_TOF-Phase2). Since then, many measurements have been performed [20], starting with a series for the commissioning and characterization of the neutron beam, which are discussed in this paper. Everything in this manuscript refers to the n\_TOF facility after the 2008 upgrade, except when is explicitly specified that something refers to the previous configuration n\_TOF-Phase1 (2001–2004).

The knowledge of every parameter describing the neutron beam is essential for the accurate analysis of experimental data. To this aim, an extensive measurement campaign was undertaken in order to determine these parameters. A significant part of the work presented herein deals with the estimation of the uncertainties of each of the beam parameters and their effect when propagated to the different types of measurements. A brief description of the facility is given in sect. 2, which is followed by a discussion of the Monte Carlo simulations of its performance in sect. 3. The characteristics of the beam discussed in this paper are the flux and its neutron energy dependence (sect. 4), the distribution of the neutron beam in space (sect. 5) and time (sect. 6), and the in-beam background components (sect. 7).

## 2 Description of the CERN n\_TOF facility

A detailed technical description of the n\_TOF facility will be given in a dedicated paper (ref. [14]), thus only a brief summary is given in this paper.

The n\_TOF facility is part of the fixed target experimental program at the CERN accelerator complex [21], as sketched in fig. 1. At n\_TOF, a high-intensity neutron pulse is produced every 1.2 seconds (or multiples of this interval) from spallation reactions induced by a pulse of  $7 \times 10^{12}$  protons of 20 GeV/c momentum impinging on a 1.3 tonne cylindrical lead target 40 cm in length and 60 cm in diameter, which is illustrated in fig. 2. A 1 cm water layer cools the target and, together with a subsequent layer of 4 cm of water or borated water ( $\text{H}_2\text{O} + 1.28\%\text{H}_3\text{BO}_3$ , fraction in mass), moderates the initially fast neutrons into the desired energy spectrum, which ranges down to thermal energies. This separation of the cooling/moderation circuit in two regions is one of the main differences and advantages (see sect. 7.1) with respect to the previous configuration (2001–2004) where a sole water layer of 5.7 cm was used both as coolant and neutron moderator.

The experimental area begins at 182.3 m from the spallation target and has a length of 7.9 m. Along the evacuated beam line, sketched in fig. 3, a sweeping magnet (200 cm long, 44 cm gap and 3.6 Tm field) deflects the

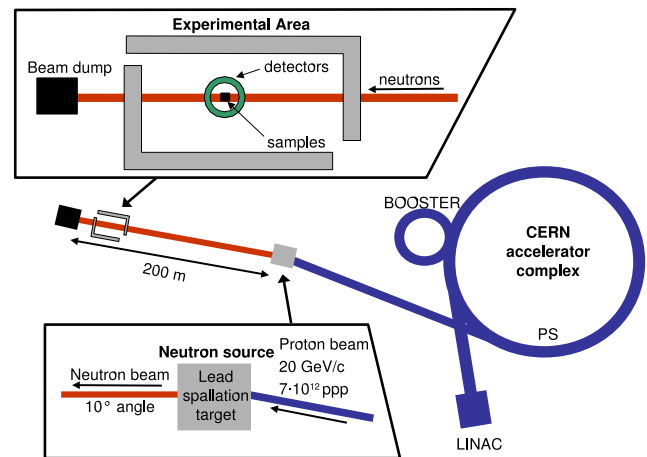


**Fig. 1.** Layout of the n\_TOF facility within the CERN accelerator complex [21]. The LINAC feeds the PS-Booster, which provides the PS with protons of 1.4 GeV/c for acceleration up to 20 GeV/c. This beam is extracted and sent to the n\_TOF lead spallation target in bunches of  $7 \times 10^{12}$  protons. The experimental hall is located near the end of the 200 m long neutron beam line.

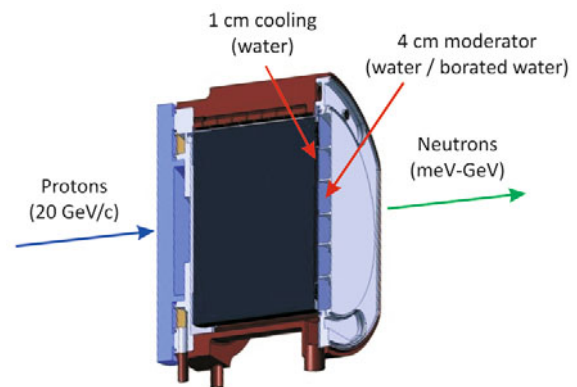


**Fig. 2.** Cross section of the n\_TOF lead spallation target. The separation of the cooling (water) and moderator (water or borated water) layers is realized by a thin aluminium window.

charged particles in the beam and two collimators shape the neutron beam. The diameter of the second collimator, placed at 178 m from the spallation target, can be chosen between 18 mm (*capture* mode with 235 cm of steel plus 50 cm of borated polyethylene) and 80 mm (*fission* mode with 50 cm of borated polyethylene plus 125 cm of steel plus 75 cm of borated polyethylene) to accommodate the needs of each measurement.

Several detection systems are available to study different types of reactions. Liquid ( $\text{C}_6\text{D}_6$  [22]) and solid ( $\text{BaF}_2$  [23]) scintillators are used to measure the  $\gamma$ -rays following  $(n, \gamma)$  reactions, while gas (MicroMegas [24, 25]) and solid-state (silicon [26] and diamond [27]) detectors are employed for  $(n, \text{charged-particle})$  reaction measurements. Lastly, fission reactions are measured with gas detectors (MicroMegas [24, 25] and PPAC [28]). The combination of these detection systems with a fully digital Data

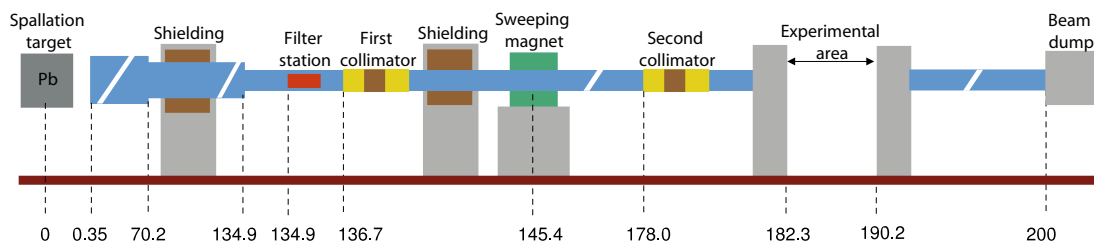


**Fig. 3.** Layout of the n\_TOF neutron beam line from the spallation target to the beam dump (distances are given in meters).

Acquisition System [29] has enabled the accurate measurement of a large number of cross sections (the complete list of published results can be found on the n\_TOF website [www.cern.ch/nTOF](http://www.cern.ch/nTOF)) and several key technical contributions [22,30–32] to this field of research in the last decade.

### 3 Monte Carlo simulation of the facility

Monte Carlo simulations are used for determining the characteristics of the neutron beam. In particular, once they are validated with experimental data, simulations give access to information that cannot be measured with the required accuracy (experiments always have limitations in terms of statistics and sizeable backgrounds are sometimes unavoidable) or is simply not accessible through experiments (see, for instance, the discussion on the resolution function in sect. 6).

This section deals with the technical details of the simulations, while the results and their comparison with experimental data are discussed throughout the corresponding sections later in this paper.

#### 3.1 FLUKA and MCNP simulations

Since the start-up of the n\_TOF facility in 2001, the geometry of the facility has been implemented in FLUKA [33, 34] in considerable detail. However, for neutronics calculations only the region around the spallation target illustrated in fig. 4 is important, since the surrounding structures are only important for estimating the activation of materials, residual dose, etc. The changes made during the upgrade period (2004–2008), particularly the new spallation target assembly, are included in the simulated geometry, which was also exported to MCNP [35] using the built-in feature in FLAIR [36], the FLUKA Graphical User Interface.

The choice of using both FLUKA (version 2011) and MCNP (MCNPX version 2.6) was made in order to take advantage of each code's strong points in a study where a variety of particle interactions, spanning at least 12 orders of magnitude in energy, are followed. In particular, FLUKA boasts very accurate and well-benchmarked high-energy hadron interaction models, appropriate for simulating the proton beam interaction with the spallation target. Nevertheless, the transport of neutrons below

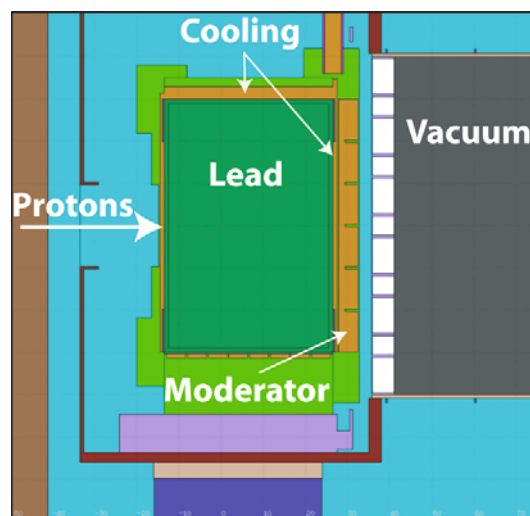


**Fig. 4.** Geometry of the target assembly implemented in the FLUKA and MCNP simulations (partial view).

20 MeV (and down to the lowest threshold of 0.01 meV) is performed by a multi-group algorithm and an associated grouped cross section library containing over 250 materials. The above-mentioned energy range is subdivided into 260 groups of approximately equal logarithmic width where inelastic reactions are not simulated explicitly, but treated as transfer probabilities between energy groups, forming a so-called *downscattering matrix*. While this approach is generally reliable and very CPU-efficient, it can lead to unphysical artifacts when studying thin and/or low density objects or when the resonance structure of the studied material is relevant to the problem (*e.g.* in shielding applications). This implies a limitation, for instance, in extracting accurate information on the resonance absorption dips present in the n\_TOF neutron energy spectrum. It is in this context that MCNP becomes useful, since it employs point-wise neutron cross sections down to thermal energies.

#### 3.2 Neutron production: geometry and scoring

The geometry was carefully built based on technical documentation of the n\_TOF facility (spallation target, vacuum windows, ...) and civil engineering layouts of the environment (tunnels, target area, ...). Furthermore, the

composition of the materials and especially of the aluminium alloys which constitute the various windows and beam-line components were defined in the best possible detail taking into account the available specifications and their chemical and isotopic composition. The goal of the simulations was to follow the proton beam interaction with the lead spallation target, and to track all particles produced, up to a scoring plane corresponding to the entrance of the neutron beam line vacuum tube. In particular, the neutron or  $\gamma$ -ray position, direction, energy, weight and time of arrival (defined as the time between the primary proton hitting the target and the secondary particles reaching the scoring plane) were recorded for their subsequent transport through the beam line. Particles entering the vacuum tube at an angle greater than  $10^\circ$  relative to the beam-line axis were immediately discarded as they can never reach the experimental area. All this information was later used to study the neutron propagation towards the experimental area, as described in sect. 3.3.

### 3.3 Neutron transport along the beam line

A full simulation of the neutrons travelling along the beam-line up to the experimental area would be impractical since the solid angle subtended by the second collimator is less than  $10^{-8}$  sr. Such calculations would therefore require an unaffordable long CPU time.

To address this issue, an independent external code was developed which uses the information obtained from the simulations to carry out the propagation of the neutrons or  $\gamma$ -rays to the experimental area *a posteriori*. To this aim, a variance reduction algorithm was implemented. The latter assumes that within a sufficiently small angle  $\theta_{cut}$  (relative to the beam axis) neutrons are emitted isotropically throughout the full energy range. In general, this is not true: high-energy neutron emission is (strongly) forward-peaked, while the angular distribution of thermal neutrons is largely isotropic. Nevertheless, the assumption holds within a small forward angle ( $\theta_{cut} = 5^\circ$ ), and thus a conservative value of  $\theta_{cut} = 3^\circ$  was used for these calculations.

The first step is to project each neutron trajectory and determine its hitting point at a distance  $L$  corresponding to the experimental area (without accounting for any collimation) and discard all those that arrive outside a circle of radius  $L \times \tan \theta_{cut} + 0.4$  m, (e.g.  $183 \text{ m} \times \tan 3^\circ + 0.4 \text{ m} = 10.0 \text{ m}$ ), where the 0.4 m radius of the vacuum tube after the lead target (*i.e.* the neutron scoring plane) is included to account for the beam halo. The remaining neutrons are the ones assumed to be emitted isotropically. Subsequently, a scoring surface in the experimental area is selected, defined by its position along the line (e.g. 183 m) and its radius (e.g. 2 cm). This surface is meant to represent a sample or detector. A scoring grid (1 mm step) is defined on this surface and, for each neutron, a trajectory is calculated to each point on this grid starting from its initial position at the beginning of the vacuum tube. For each instance of the neutron (*i.e.* for

each calculated trajectory) the program checks if the trajectory *hits* either a tube or collimator (see fig. 3). If so, this neutron is considered not to reach the experimental area and is thus rejected. In the opposite case, it is scored. The final result is appropriately normalized to provide the neutron flux and the spatial beam profile at the scoring surface in the experimental area.

In calculating the neutron trajectories, the program was designed to account for the effect of gravity. While fast neutrons are practically unaffected over a  $\sim 185$  m flight path, the effect is visible for thermal neutrons (3 cm vertical drop along 185 m) and has a measurable impact on the spatial profile of low energy neutrons (more details are given in sect. 5).

## 4 Neutron flux

The neutron flux is here defined as the number of neutrons per incident proton pulse and integrated over the full spatial beam profile arriving at the experimental hall with a given energy. Its absolute value and energy distribution as well as the associated uncertainties are essential for the analysis of cross section data obtained via the time-of-flight technique. The accuracy with which the neutron flux is determined may indeed become the limiting factor in the accuracy achievable in a cross section experiment and therefore must be improved as much as possible. The knowledge of the dependence of the neutron flux on energy is similarly important as knowing its absolute value because reaction cross sections are usually measured relative to some well known quantity in a particular energy range, e.g. a standard cross section, the cross section value at thermal energies, or the capture yield at the top of a well isolated saturated resonance [37].

In the case of n\_TOF, we have experimentally determined the neutron flux using several detection systems based on different principles and reactions. These are included in the analysis only in the energy region where the associated cross sections are well-established standards [38]. The measurements, their analysis and their combination for the determination of the *evaluated neutron flux* are discussed in the following sections. A manuscript with even further details about each measurement and the neutron flux evaluation process is currently under preparation [39].

### 4.1 Methodology and measurements

The determination of the neutron flux is based on the relation between the measured reaction yield  $Y_x^{meas}$  and the expected (theoretical) value  $Y_x^{th}$  calculated from the corresponding standard cross section. The former is calculated from measurable quantities as

$$Y_x^{meas}(E_n) = \frac{C(E_n) - B(E_n)}{\varepsilon_x(E_n) \times \Phi_n(E_n)}, \quad (4)$$

where  $C$  and  $B$  are the total and background counts per neutron pulse,  $\varepsilon_x$  is the detection efficiency for the re-

action of interest, and  $\Phi_n$  is the neutron flux to be determined. All these observables, as explicitly indicated in eq. (4), are neutron energy dependent. The expected yield is calculated, to a first approximation (without considering multiple scattering), from the characteristics of the sample used in the measurement and the associated cross section as

$$Y_x^{th}(E_n) = \left(1 - e^{-n\sigma_t(E_n)}\right) \frac{\sigma_x(E_n)}{\sigma_t(E_n)}, \quad (5)$$

where  $n$  is the areal density of the sample in atoms-per-barn and  $\sigma_t$  and  $\sigma_x$  are the total and reaction cross sections expressed in barns, respectively. When the sample is sufficiently thin, the self-shielding becomes negligible and thus a combination of the two previous equations allows calculating the neutron flux as

$$\Phi_n(E_n) = \frac{C(E_n) - B(E_n)}{\varepsilon_x(E_n) \times n \times \sigma_x(E_n)}. \quad (6)$$

We have determined the neutron flux of n\_TOF applying this methodology to several dedicated measurements. By combining these independent measurements in a consistent way, it was possible to determine the neutron flux between thermal and 1 GeV with rather small systematic and statistical uncertainties. The detectors for charged particles SiMon [26] and MGAS [24, 25] have been used for measuring  $(n, \alpha)$  reactions on thin  ${}^6\text{Li}$  and  ${}^{10}\text{B}$  foils, which feature standard cross sections from 25 meV to 1 MeV. In addition, the detectors H19 from PTB [40], MGAS [24, 25] and PPAC [28] have all been used to measure  ${}^{235}\text{U}(n, f)$  reactions, whose cross section is standard at 25 meV and in the interval between 150 keV and 200 MeV. This reaction has also been used as reference above 200 MeV, due to the absence of any standard cross section at such high energies.

As an illustrative example of the responses of the detectors to the mentioned reactions, fig. 5 shows some pulse height distributions in the neutron energy range between 0.1 and 10 eV. The labels indicate the origin of the structures that are observed in each case and the dashed vertical lines indicate the analysis gates selected for the identification of the reaction products of interest. These gates, shown here only in the eV region, are neutron energy dependent and have been determined carefully for the analysis of the flux in the complete neutron energy range.

As mentioned previously, all the measurements performed to determine the neutron flux are based on reactions whose cross sections are standards in particular energy regions [38], as summarized in table 1. The table presents also the energy regions where each detector provides reliable data. For instance, the uncertainties in the angular distribution of the reaction products from the  ${}^6\text{Li}(n, \alpha)$  reaction limit the use of the *SiMon* detector to energies below  $\sim 150$  keV, while the effects of the  $\gamma$ -flash (see sect. 7.2) limits the use of the H19(PTB) and MGAS( ${}^{235}\text{U}$ ) fission chambers beyond  $\sim 3$  and  $\sim 10$  MeV, respectively. In the case of MGAS( ${}^{10}\text{B}$ ), the background caused by proton recoils from elastic n-p collisions in the gas limits the high energy range up to only few hundreds of keV.

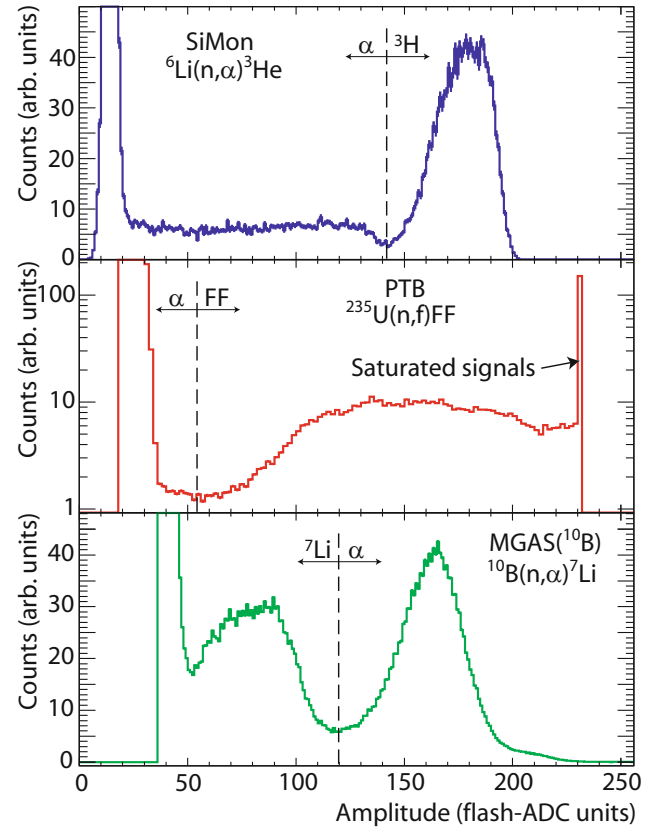


**Fig. 5.** Distribution of pulse heights corresponding to some of the detectors (and covering the three reaction types of interest) involved in the experimental determination of the n\_TOF neutron flux.

Taking these energy limits into account, the neutron flux has been derived from eq. (6) as described in the following section.

## 4.2 Evaluated neutron flux

To evaluate the neutron flux, the results from each individual measurement have been combined and the overall uncertainty has been estimated consistently. Taking into consideration that the efficiency of the H19 fission detector from PTB and the mass of the corresponding samples are the best known quantities (see ref. [40]), the fluxes measured with the other detectors have been normalized to the PTB detector at 25 meV, where all the measured reactions have standard cross sections. The evaluated neutron flux has then been obtained as a weighted average of the individual fluxes, including in each energy range only those whose associated cross section is standard and considering the reliable energy intervals mentioned in table 1.

The results are displayed with a 100 bins per decade in the upper panel of fig. 6, where the wide range of neutron energies provided by the n\_TOF neutron beam is clearly visible. The two fluxes displayed correspond to the capture collimator mode in the configurations with water and borated water as moderators. In all cases the MeV

**Table 1.** Summary of the detectors used for the determination of the neutron flux, including the reactions of interest, the energy range in which their cross section is considered standard, the sample thicknesses, the collimator used, and the (approximate) upper energy limit for proper operation of each detector.

| Detector | Sample and reaction                 | Areal density ( $\mu\text{g}/\text{cm}^2$ ) | Collimation (diameter in mm) | $E_n$ where $\sigma_x$ is standard | Upper $E_n$ limit for detection <sup>(a)</sup> |
|----------|-------------------------------------|---|------------------------------|------------------------------------|--|
| PTB      | $^{235}\text{U}(\text{n},\text{f})$ | 500 (10 samples)                            | Capture (18)                 | 25 meV, 0.15–200 MeV               | 3 MeV  |
| SiMon    | $^6\text{Li}(\text{n},\text{t})$    | 300   | Capture (18)                 | 25 meV to 1 MeV                    | 150 keV  |
| MGAS     | $^{10}\text{B}(\text{n},\alpha)$    | 55  | Capture (18)                 | 25 meV to 1 MeV                    | 150 keV  |
| MGAS     | $^{235}\text{U}(\text{n},\text{f})$ | 470   | Capture (18)                 | 25 meV, 0.15–200 MeV               | 1 MeV  |
| PPAC     | $^{235}\text{U}(\text{n},\text{f})$ | 279   | Fission (80)                 | 25 meV, 0.15–200 MeV               | 1 GeV  |

(a) See text for details.

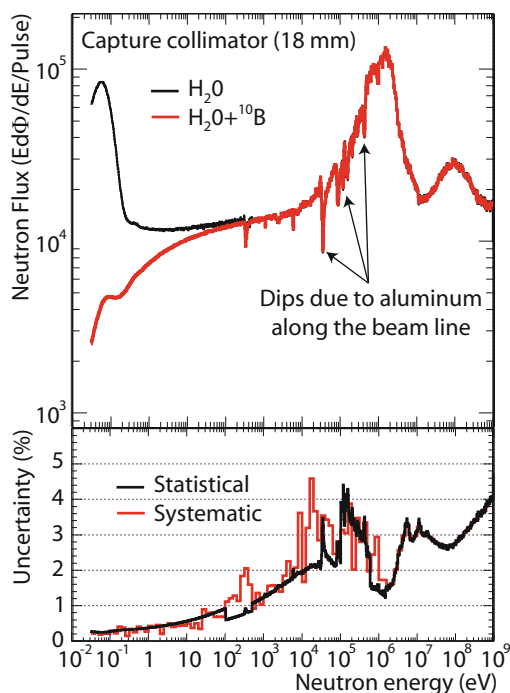


**Fig. 6.** Top: Evaluated neutron flux in the configuration with the capture collimator (18 mm diameter) with water and borated water as moderator. Bottom: Systematic and statistical uncertainties (see text for details).

region shows the typical neutron evaporation spectrum, with the intermediate region containing the partially moderated neutrons and the low-energy region, corresponding to thermalized neutrons, changing significantly when borated water is used instead of normal water due the higher neutron absorption probability through  $^{10}\text{B}(\text{n},\alpha)$  than through  $^1\text{H}(\text{n},\gamma)$  reactions. This also leads to a reduction of the intensity and energy of the in-beam  $\gamma$ -ray background, as discussed in sect. 7.1. The region between 20 keV and 1 MeV features a series of dips, which are transmission dips associated to resonances in the aluminium windows of the spallation target assembly and at both ends of the evacuated flight path. These resonance dips have a sizable effect when measuring the cross section of isotopes with resonances at such high energies, but

**Table 2.** Number of neutrons per pulse, assuming a nominal pulse intensity of  $7 \times 10^{12}$  protons per pulse), in different neutron energy ranges in the capture and fission collimator modes using water and borated water as moderator.

| Neutron energy | Neutrons/pulse                      |                                     |                                     |
|----------------|-------------------------------------|-------------------------------------|-------------------------------------|
|                | Capture mode                        |                                     | Fission mode                        |
|                | $\text{H}_2\text{O}$                | $\text{H}_2\text{O}+^{10}\text{B}$  | $\text{H}_2\text{O}+^{10}\text{B}$  |
| 10–100 meV     | $1.0 \times 10^5$                   | $1.5 \times 10^4$                   | $3.3 \times 10^5$                   |
| 0.1–1 eV       | $4.3 \times 10^4$                   | $1.3 \times 10^4$                   | $2.9 \times 10^5$                   |
| 1–10 eV        | $2.7 \times 10^4$                   | $2.0 \times 10^4$                   | $4.3 \times 10^5$                   |
| 10–100 eV      | $2.8 \times 10^4$                   | $2.5 \times 10^4$                   | $5.3 \times 10^5$                   |
| 0.1–1 keV      | $2.9 \times 10^4$                   | $2.9 \times 10^4$                   | $6.2 \times 10^5$                   |
| 1–10 keV       | $3.2 \times 10^4$                   | $3.2 \times 10^4$                   | $6.8 \times 10^5$                   |
| 10–100 keV     | $4.4 \times 10^4$                   | $4.4 \times 10^4$                   | $9.4 \times 10^5$                   |
| 0.1–1 MeV      | $1.3 \times 10^5$                   | $1.3 \times 10^5$                   | $2.7 \times 10^6$                   |
| 1–10 MeV       | $1.5 \times 10^5$                   | $1.5 \times 10^5$                   | $3.1 \times 10^6$                   |
| 10–100 MeV     | $5.0 \times 10^4$                   | $5.0 \times 10^4$                   | $1.0 \times 10^6$                   |
| 0.1–1 GeV      | $4.7 \times 10^4$                   | $4.7 \times 10^4$                   | $9.5 \times 10^5$                   |
| <b>Total</b>   | <b><math>6.8 \times 10^5</math></b> | <b><math>5.5 \times 10^5</math></b> | <b><math>1.2 \times 10^7</math></b> |

only slightly affect the measurement of actinides and their unresolved resonance cross section in this region.

The number of neutrons per pulse (corresponding to  $7 \times 10^{12}$  protons) integrated over energy decades are given for each collimator and moderator configurations in table 2. The total number of neutrons per pulse varies between  $5.5 \times 10^5$  and  $12 \times 10^6$ , depending on the collimator/moderator configuration.

Regarding the statistical and systematic uncertainties in the neutron flux, displayed in the bottom panel of fig. 6, the former has been calculated through standard uncertainty propagation and the latter has been estimated as the Root Mean Square (RMS) of the values that are included in the averaging at each neutron energy bin. In this way, the lower limit for the systematic uncertainty is given by the statistical one. Indeed, it is observed that the systematic uncertainty is larger than the statistical only

near the large aluminium dip around 20–30 keV. Overall, the neutron flux with 100 bins per decade has been determined within 1% uncertainty between thermal and 100 eV, 2% between 100 eV and 10 keV, 3–4% between 10 keV and 1 MeV, and 2–3% between 1 and 200 MeV. Above 200 MeV the  $^{235}\text{U}(n,f)$  cross section is not standard and therefore we can only report the statistical uncertainty of our flux, which varies between 3 and 4%. These uncertainty values constrain the maximum accuracy that can be reached in absolute cross section measurements at n\_TOF; however, the results from both fission and capture cross section measurements can reach higher accuracies if performed relative to standard cross sections such as  $^{197}\text{Au}(n,\gamma)$  or  $^{235}\text{U}(n,f)$ .

### 4.3 Consequences of a high instantaneous flux

Many of the measurements carried out at n\_TOF are made on radioactive samples such as actinides ( $^{233}\text{U}$ ,  $^{240,242}\text{Pu}$ ,  $^{241,243}\text{Am}$ ,  $^{245}\text{Cm}$ , ...), fission products ( $^{93}\text{Zr}$ ,  $^{151}\text{Sm}$ , ...) and others ( $^{59}\text{Ni}$ ,  $^{63}\text{Ni}$ , ...). In these cases, the activity of the sample itself often becomes the dominant source of background. At n\_TOF, due to the very high instantaneous intensity of each neutron pulse, the contribution of the sample-activity background to the measurement is largely reduced with respect to other facilities.

As an example fig. 7 shows the counting rate recorded with a pair  $\text{C}_6\text{D}_6$  scintillators in the  $(n,\gamma)$  measurement of a 32 mg  $^{241}\text{Am}$  sample [41, 42]. The activity of this sample was 4 GBq, and even with such a high activity the measurement could be carried out at n\_TOF with a favorable capture-to-background ratio in the complete energy range. The example also serves to illustrate the wide neutron energy range, between thermal and 1 MeV, fully covered in each pulse at n\_TOF thanks to its uniquely short duty cycle.

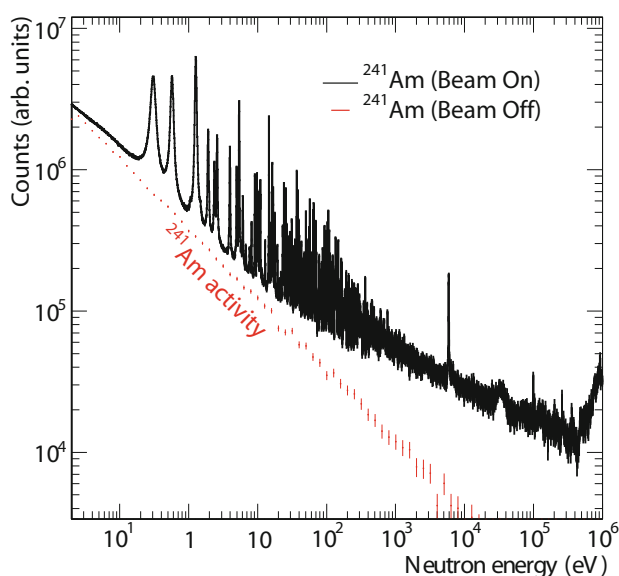


**Fig. 7.** Neutron energy distribution corresponding to the measurement of  $(n,\gamma)$  reactions from a 32 mg  $^{241}\text{Am}$  sample with an activity of 4 GBq.

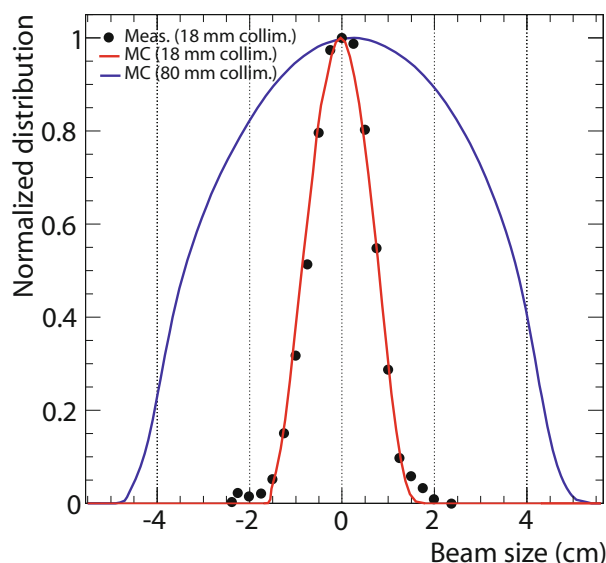


**Fig. 8.** Neutron beam profile at 183.2 m in the vertical direction as measured with the pixel-MGAS detector at low neutron energy (0.1–1 eV).

## 5 Spatial beam profile

The spatial profile of the neutron beam at the sample position is mainly shaped by the characteristics of the second collimator. The two collimation modes available at n\_TOF (see sect. 2) obviously provide neutron beams of different size. Furthermore, the beam profile varies with the energy of the neutrons because neutrons of different energies are produced at different positions and emitted at different angles from the spallation target and thus follow different paths during their moderation in the target and the cooling/moderator system. The knowledge of this spatial profile is essential for the accurate measurement of cross sections and is of particular importance when the sample being measured is smaller than the neutron beam and therefore intercepts only a fraction of it, referred to as the Beam Interception Factor (BIF).

The spatial profile of the neutron beam and its energy dependence in the capture collimator configuration were already investigated in detail in n\_TOF-Phase1 by means of a 1D-stripped MicroMegas detector (see ref. [43] for details). The results were found to be in agreement with simulations available at the time. In the present n\_TOF configuration, a new 2D pixelated MicroMegas (pixel-MGAS) detector has been developed [44]. This new detector, with a 5 cm diameter active area including 308 square pixels of 2.5 mm side read out by 4 Gassiplex cards, has provided in 2012 results compatible with those measured in 2001 with the stripped-MGAS detector.

An illustration of the n\_TOF beam profile at 183.2 m flight path is given in fig. 8, where the beam projection in the vertical direction for neutron energies between 0.1 and 1 eV is shown for both capture and fission collimator modes. The capture mode includes both the measurement with the pixel-MGAS and simulations (see sect. 3.1), which are in good agreement except in the tails of the dis-

tribution, where the measured data are affected by background. In the fission mode, only the simulations are available. It is observed that the full size of the beam is  $\sim 3.5$  cm and  $\sim 10$  cm in diameter in the capture and fission collimation modes, respectively.

### 5.1 Beam interception factor

The value of the BIF at 183.2 m flight path using the capture collimator has been calculated from the validated simulations for typical sample diameters of 1, 2, 3 and 4 cm, always considering samples that are perfectly aligned with the beam line.

The results are shown in fig. 9, where the BIF values in the eV region are 0.21, 0.68, 0.96 and 1.0 for samples with diameters of 1, 2, 3 and 4 cm, respectively. Figure 9 clearly shows the slight variation of the BIF with neutron energy which needs to be accounted for when the cross section measurements are normalized in a particular neutron energy region. The difference between the BIF value at 4.9 eV (which is the usual normalization point for capture experiments at n\_TOF via the saturated resonance method [37] with  $^{197}\text{Au}$ ) and the values at thermal and at 300 keV reaches 2.5% for samples of only 1 cm diameter, and is less than 1.5% for samples with a diameter larger than 2 cm. The figure also includes 4 lines around the BIF values for 2 cm diameter that correspond to the values for a sample misaligned by 1 mm upwards, downwards, left and right. These results show that an accurate sample alignment is crucial, since a misalignment of just 1 mm can lead to a deviation of several percentage points with respect to the BIF value at the nominal sample position.

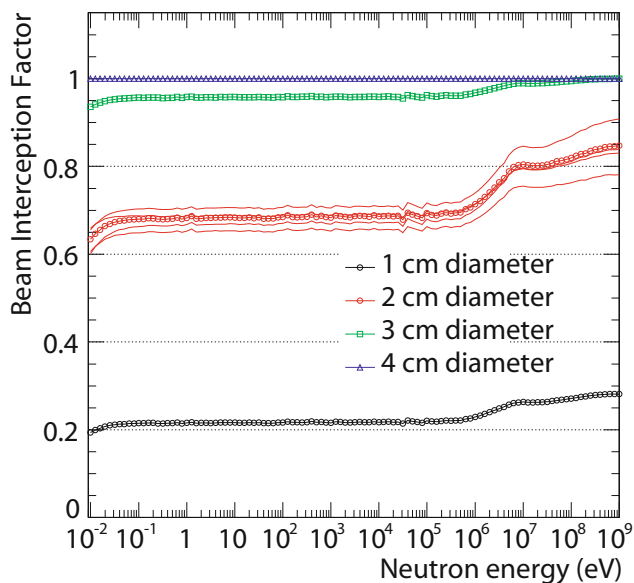


**Fig. 9.** Simulated beam interception factor BIF (at 183.2 m flight path) as a function of neutron energy for circular samples 1 to 4 cm in diameter. The four thin lines around the 2 cm diameter values correspond to sample misalignments of  $\pm 1$  mm horizontally and vertically.

The effect is indeed larger in the case of a vertical misalignment, which is explained by the effect of gravitation on thermal neutrons, since it takes them more than 100 ms to reach the experimental area.

Overall, it can be concluded that the variation of the BIF with neutron energy must be considered in data analysis when measuring samples smaller than the beam, considering as well that any possible misalignments of the sample could imply an uncertainty on the neutron energy dependence of the BIF, and thus in the corresponding measured cross section, which can reach a maximum of 2.5% at thermal energies for samples with a diameter of only 1 cm.

### 6 Resolution function and ToF/ $E_n$ relation

The resolution function describes the distribution of the measured time of flight for neutrons with a given kinetic energy. Several experimental conditions like the primary beam pulse duration (7 ns RMS in the case of n\_TOF), the moderation time in the target-moderator assembly, and the detector response, contribute to the fact that the time of flight  $t$  and the flight length  $L$  for a neutron of energy  $E_n$  in eq. (2) are not fixed values but merely distributions. The convolution of these distributions is known as the resolution function  $R_E(E_n)$  for a given incident neutron energy and can be easily transformed in equivalent distributions in either energy, time, or distance by using the conservation of probability

$$R_E(E_n)dE_n = R_t(t)dt = R_L(L)dL, \quad (7)$$

where  $E_n$ ,  $L$  and  $t$  are related to each other through eq. (2). Since the energy dependence of the equivalent distance  $R_L(L)$  is weaker than  $R_t(t)$  and  $R_E(E)$ , this form is often used to represent resolution functions graphically. Although the resolution function cannot be measured directly, it is assessed either by an analytical approach of its components or, more commonly, by Monte Carlo simulations. The resolution function can then be validated by measurements of well-known resonances.

The resolution function is usually non-Gaussian and even asymmetric which does not only alter the shape of resolved resonances, but also changes the time-energy calibration with energy, as a consequence of a shift in the observed resonance peak position. For resolved resonances analyzed with  $R$ -matrix codes like SAMMY [45] or RE-FIT [46], a parametrization of the resolution function or a numerical representation is used to fit the resonance shape and its position. The combination of an arbitrary geometrical flight length  $L$  and the also arbitrary center of the resolution function results in the time-energy calibration. Usually, but not necessarily, the resolution function starts at zero equivalent distance, and the geometrical flight length is calibrated accordingly with a well-known low-energy resonance.

For reaction yields at higher energies where no resolved resonances are present, the conversion of time to energy with eq. (2) uses the effective flight length  $L_{\text{eff}}$  which

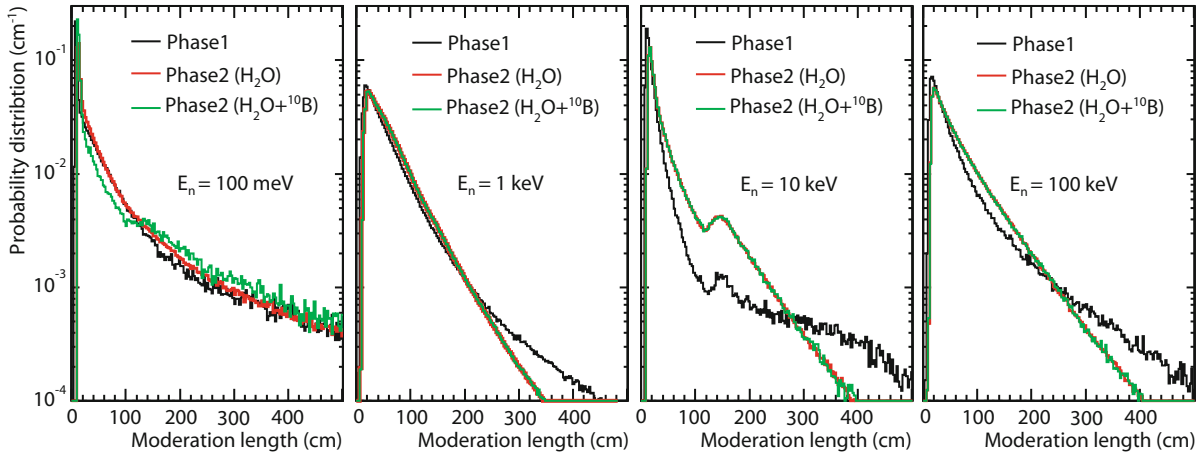


**Fig. 10.** Comparison of the resolution functions, in the form of equivalent distance at different neutron energies in the meV to keV regions, corresponding to n\_TOF-Phase1 and Phase2.

is the sum of the previously described fixed value of  $L$  and a mean moderation length  $\int LR_L(L)dL$ . In some approximations, where the mean value ( $\lambda$ ) follows a simple parametrized energy dependence, it is possible to simplify the time-energy calibration as explained in [31].

### 6.1 The n\_TOF resolution function

The resolution function of the n\_TOF facility has been simulated in the start-up phase by two different codes, FLUKA [13] and CAMOT [47], giving similar results within the available statistics. In the second phase of n\_TOF, the new spallation target assembly has been simulated again with FLUKA and also with MCNP for the two moderator configurations. These three resolution functions are displayed in fig. 10 in the form of moderation length at different neutron energies. The first panel shows the large differences between the various configurations for slow neutrons. However, at such low neutron energies Doppler broadening dominates over the resolution broadening (see discussion in sect. 6.2) and is thus not important. At higher energies, in the keV region, there are essentially no differences between the two configurations (use or not of borated water as moderator) of n\_TOF-Phase2, but there are sizable differences with respect to Phase1. The increase in the width of the resolution at energies above 1 keV is associated with the presence of additional aluminium windows (to separate the cooling and moderator circuits) and the air gap existing in n\_TOF-Phase2 between the spallation target and the evacuated beam line.

In n\_TOF-Phase1, the simulated resolution function results were used to derive an analytical description in the range from 1 eV to 1 MeV [48] given by

$$R_t(t) = A_0 e^{-\frac{t-\tau}{\lambda}} \frac{(t+\tau)^2}{2!A^3} + A_0 A_1 \left( A_2 e^{-A_3(t+t_0)\sqrt{E}} + A_4 e^{-A_5(t+t_0)\sqrt{E}} \right), \quad (8)$$

**Table 3.** Values of the resolution function widths and corresponding energy resolution (calculated from eq. 3 using the FWHM) as function of neutron energy for the configuration with borated water as moderator.

| $E_n$ (eV) | FWHM (cm) | FWTM (cm) | $\Delta E_n/E_n$     |
|------------|-----------|-----------|----------------------|
| 1          | 3         | 8         | $3.2 \times 10^{-4}$ |
| 10         | 3         | 8         | $3.2 \times 10^{-4}$ |
| $10^2$     | 4         | 11        | $4.3 \times 10^{-4}$ |
| $10^3$     | 5         | 16        | $5.4 \times 10^{-4}$ |
| $10^4$     | 10        | 41        | $1.1 \times 10^{-3}$ |
| $10^5$     | 27        | 107       | $2.9 \times 10^{-3}$ |
| $10^6$     | 49        | 106       | $5.3 \times 10^{-3}$ |

where  $A$ ,  $\tau$ ,  $A_0$ ,  $A_1$ ,  $A_2$ ,  $A_3$ ,  $A_4$  and  $A_5$  are energy-dependent parameters. This form of the resolution function is known as the modified RPI function and is present in the codes SAMMY [45] and REFIT [46] for resonance analysis. This analytical function describes reasonably well the n\_TOF-Phase1 simulations made with CAMOT and FLUKA. However, a numerical description of the n\_TOF resolution broadening has been made available in both SAMMY and REFIT codes. This allows for a more accurate description of the overall broadening and provides more flexibility at the stage of data analysis.

The values of the resolution function broadening for the configuration with water as moderator, in the form of widths at one half (FWHM) and at one tenth (FWTM) of the maximum value, are given in table 3. The FWHM varies between 3 and 50 cm, yielding a relative energy resolution that ranges between a minimum of 0.03% below 10 eV and a maximum of 0.5% around 1 MeV. The mean value of the resolution function expressed as equivalent

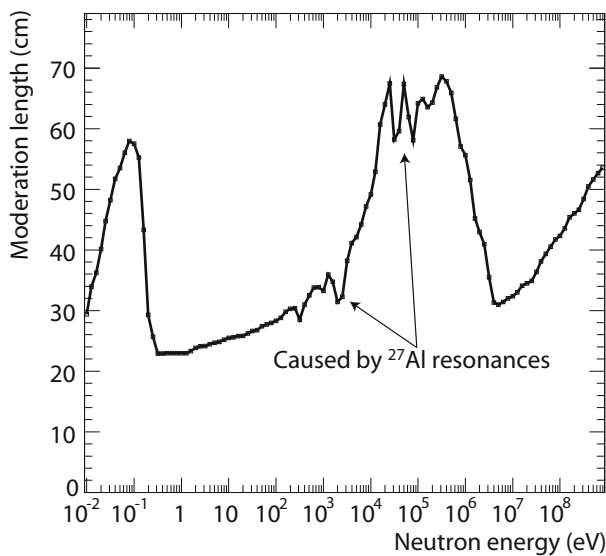


**Fig. 11.** Average value of the moderation length as a function of neutron energy, which is used for the time-to-energy conversion (see text).

moderation length is displayed in fig. 11. As mentioned before, this is understood as an effective moderation length which must thus be added to the geometrical time-of-flight distance to use the time-to-energy conversion given in eq. (2), that is  $L_{eff} = L_{geom} + \lambda(E_n)$  (see ref. [31]).

## 6.2 Effect of the resolution function in the resonance shapes

The high resolution of the n.TOF neutron beam makes it possible to observe resonances up to tens and hundreds of keV. An example is displayed in fig. 12, which shows a resonance from  $^{56}\text{Fe}$  measured near 80 keV. The calculated Doppler broadened resonance shape is shown as reference to illustrate the effect of the resolution broadening. This is indeed sizable, but still allows to accurately determine the strength of the measured resonances from their integrals, which remain unchanged by the broadening.

To further illustrate the impact of the resolution function, a number of relative widths are displayed in fig. 13 for the case of  $^{232}\text{Th}$  (figure from ref. [48]). They all correspond to the relative width at one half maximum (FWHM/ $E$ ), except for the resonance spacing where  $D_0/E$  is displayed. In the figure, the overall resonance broadening is displayed as a thick (brown) solid line, while the individual components (Doppler, resolution function and proton pulse width) are displayed as dashed lines. The overall broadening is to be compared with the intrinsic width (blue points) and resonance spacing (pink solid line) of the  $^{232}\text{Th}$  resonances from the evaluated library JEFF-3.1.2 [49]. The comparison shows that the observed width for all the resonances will be dominated by the experimental broadening, but also that the broadening remains lower than the resonance spacing up to  $\sim 20$  keV and thus neighboring resonances will be well differentiated below that energy limit.

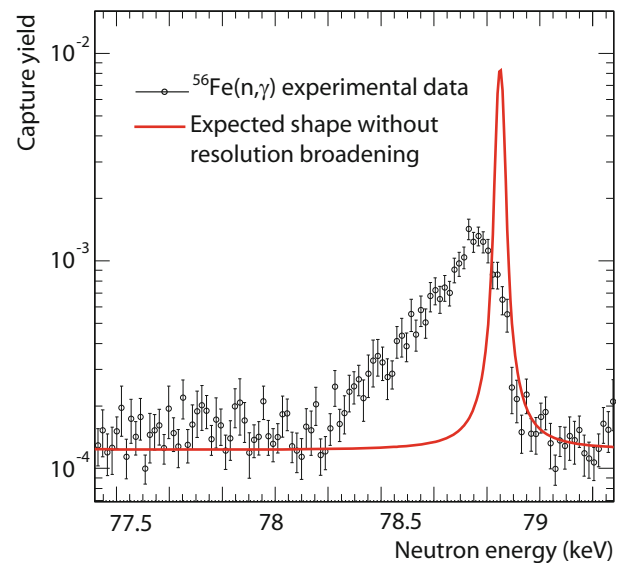


**Fig. 12.** Measured yield of a  $^{56}\text{Fe}(n,\gamma)$  resonance at 79 keV compared to the Doppler broadened resonance shape. The low energy asymmetric tail is associated to the resolution broadening, which changes the resonance shape leaving its integral unchanged.

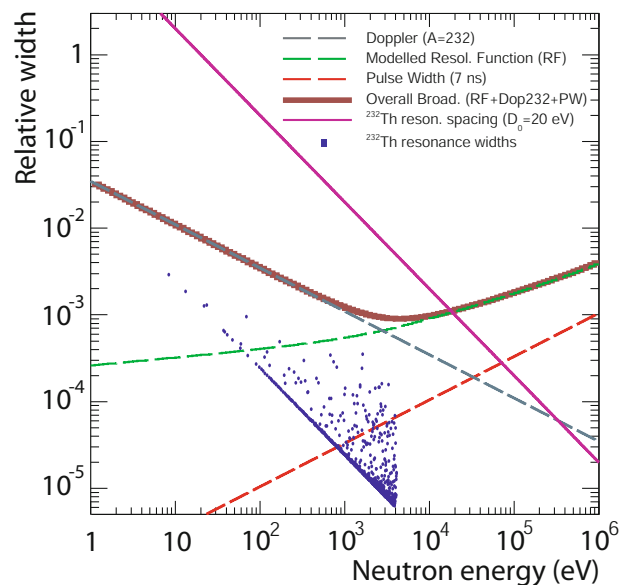


**Fig. 13.** Illustration of the experimental resonance broadening and its change as function of neutron energy. See text for a detailed explanation. (Figure after [48].)

## 7 Background conditions

### 7.1 In-beam $\gamma$ -ray background

The spallation process as well as the absorption of neutrons in the moderator are responsible for a sizable production of  $\gamma$ -rays, a fraction of which reaches the experimental hall. Knowing the energy distribution and time of flight of these photons is essential for understanding the effects of the  $\gamma$ -ray backgrounds, where a prompt and a delayed component can be distinguished.

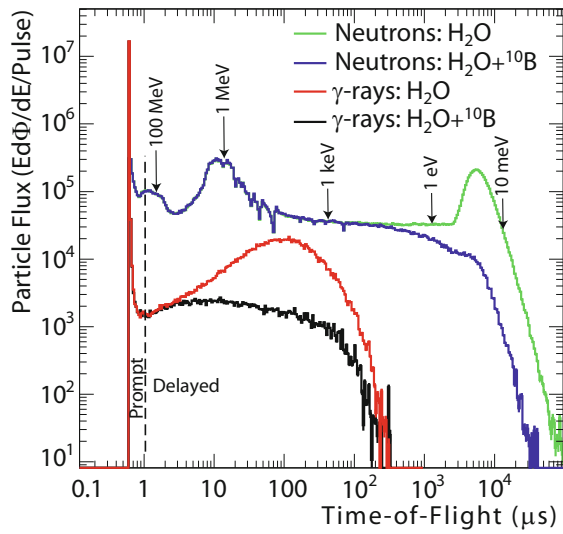


**Fig. 14.** Time of arrival of photons and neutrons in the experimental hall for the capture collimation mode in the configurations with water and borated water as moderator (labels with the corresponding neutron energy values are displayed for guidance). The large reduction of in-beam  $\gamma$ -rays in the keV neutron energy region with borated water is obvious.

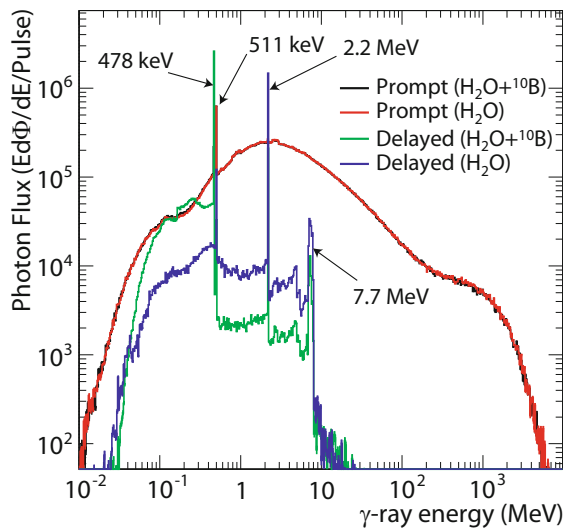


**Fig. 15.** Energy distribution of the prompt and delayed components of the in-beam photons.

Applying the same methodology described earlier for the Monte Carlo study of the neutron flux, it has been possible to obtain the information on the photon flux as well. The corresponding time-of-flight distributions of the photons arriving in the experimental hall are displayed in fig. 14. The existence of a prompt (ToF  $< 1 \mu\text{s}$ ) component arising from high-energy interactions in the target and a delayed (ToF  $> 1 \mu\text{s}$ ) component comprising mostly capture  $\gamma$ -rays from the cooling and moderator system, as well as from structural material around the spallation target, are clearly observed. The energy distribution of the  $\gamma$ -rays of these two components, displayed in fig. 15, illustrates the very different nature of the prompt and delayed  $\gamma$ -ray background. While the much larger prompt component reaches energies as high as several GeV and

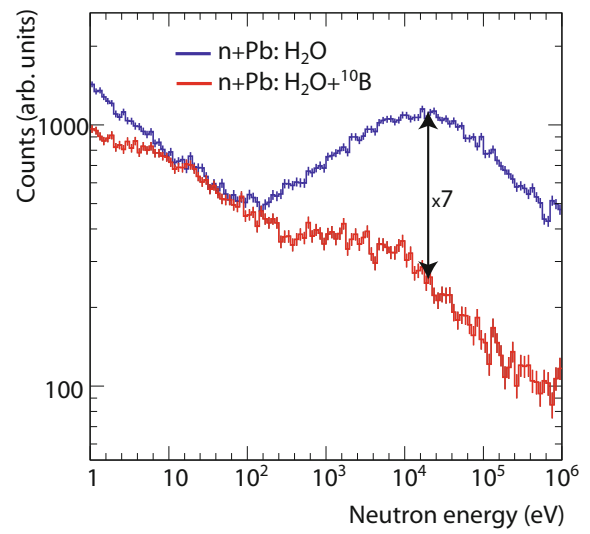


**Fig. 16.** Neutron energy distribution of events from the irradiation of a lead sample in the two moderator configurations: water and borated water. The majority of events correspond to in-beam  $\gamma$ -rays scattered at the sample and detected in the  $\text{C}_6\text{D}_6$ . The large difference above 100 eV illustrates the significant reduction of the 2.2 MeV  $\gamma$ -ray component from  $^1\text{H}(n,\gamma)$  reactions in the moderator.

does not depend on the type of moderator used, the delayed component has well-defined peaks corresponding to photons emitted in specific neutron absorption reactions in different materials. For instance, the peaks at 7.7 MeV, 2.2 MeV, 511 keV and 478 keV correspond to  $^{27}\text{Al}(n,\gamma)$ ,  $^1\text{H}(n,\gamma)$ , pair annihilation and  $^{10}\text{B}(n,\alpha)^7\text{Li}^*$  reactions, respectively.

The reduction of the 2.2 MeV  $\gamma$ -ray background by nearly one order of magnitude when using borated water as moderator is one of the main advantages of the new spallation target upgraded in 2008. In the past this background was a limiting factor in the sensitivity of some of the measurements carried out before 2004, as discussed in refs. [50,51]. Now the situation has largely improved, as illustrated in fig. 16, which shows the counting rate distributions from a measurement of a lead sample (which mainly scatters  $\gamma$ -rays and absorbs a negligible fraction of neutrons) in the two moderator configurations using, in both cases, a similar set-up based on a pair of  $\text{C}_6\text{D}_6$  detectors. The in-beam  $\gamma$ -ray background has been reduced by a factor of 7. Actually, the in-beam  $\gamma$ -ray background has not been eliminated but shifted from 2.2 MeV to 478 keV (see fig. 15), which is much less harmful because the corresponding energy deposition in the detectors, after undergoing one Compton scattering in the sample, is most of the times below the detection threshold.

## 7.2 The $\gamma$ -flash

The term  $\gamma$ -flash is commonly used to describe the prompt component of ionizing particles ( $\gamma$ -rays and others) arriving at the experimental area with the neutron beam. However, the term is somewhat misleading because the  $\gamma$ -flash

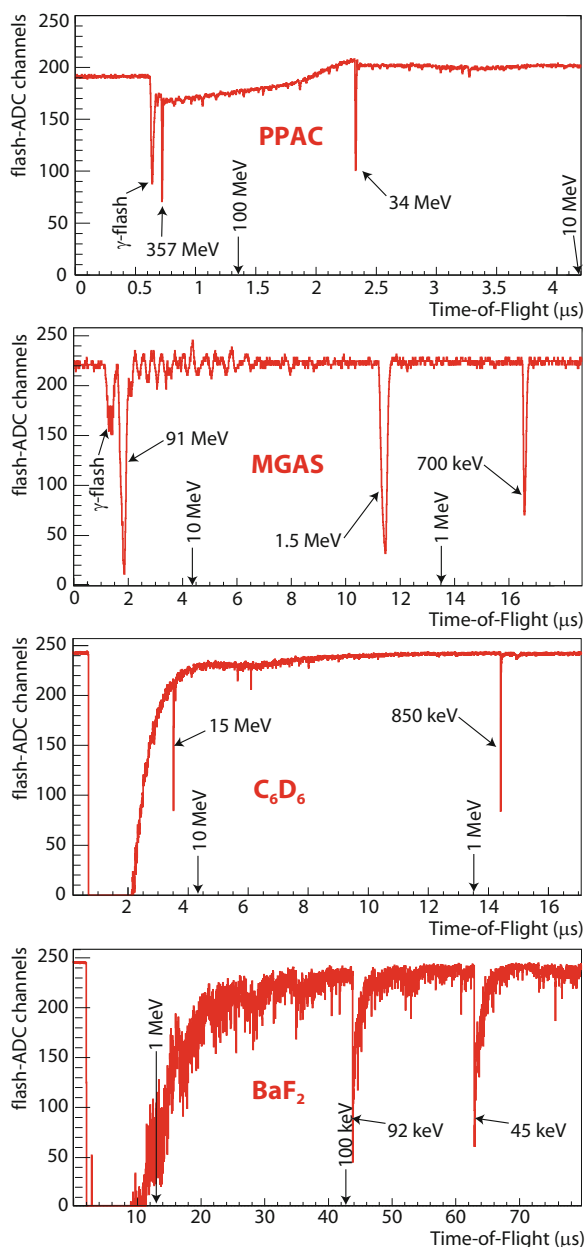


**Fig. 17.** Measured response of the PPAC, MGAS,  $C_6D_6$  and  $BaF_2$  detectors to the  $\gamma$ -flash as function of the time of flight (see text for details). A few values of the corresponding neutron energies are given for guidance.

has in fact several components, all of them observed as prompt (*i.e.*  $ToF < 1 \mu s$ ): a) charged particles produced in the spallation target, b) photons (see figs. 14 and 15) produced in the spallation target, and c) a halo of photons and charged particles produced by the interaction of the high energy neutrons and photons with the second collimator placed just upstream from the experimental hall (see fig. 3).

All these components affect each of the detectors used at n\_TOF differently, depending on the detector type and its location with respect to the beam. The situation is illustrated in fig. 17 for four different detection

systems (PPAC [28], MGAS [24,25],  $C_6D_6$  [22] and  $BaF_2$  TAC [23]), for which some useful signals following the  $\gamma$ -flash and their corresponding neutron energies are also shown. In the case of PPAC and MGAS, placed in the beam, there is always a sizable deposition of energy with the arrival of the beam which prevents one from detecting another signal until the baseline is recovered, which happens around 100 ns and 1  $\mu s$  after the beam arrival, respectively. This means that the PPAC can record fission reactions for neutron energies as high as several hundreds of MeV (1 GeV has been reported in [28]) while the MGAS operates properly below 100 MeV. In the case of the  $C_6D_6$  and  $BaF_2$  scintillators, both placed outside the beam, the response of each detector is very different, with the baselines recovering approximately 3 and 40  $\mu s$  after the arrival of the beam, respectively. These correspond to respective high energy limits of 10 MeV and 10–100 keV. When the effect of the  $\gamma$ -flash needs to be reduced in order to push measurements to higher neutron energies, one can do so by reducing the intensity of the neutron beam on demand, see, for instance, ref. [52].

## 8 Summary and conclusions

The n\_TOF facility at CERN provides a high-intensity pulsed neutron beam spanning over eleven orders of magnitude in neutron energy (thermal to 1 GeV) with a time-of-flight distance of 185 meters. The facility, devoted mainly to neutron-induced cross section measurements and operating since 2001, has been upgraded in 2008 and presently features an optimized spallation target and cooling and moderation systems.

In this paper we have presented in detail the characteristics of the neutron beam and the associated backgrounds, which are essential for the planning and analysis of measurements at n\_TOF. The results presented herein are based on measurements as well as on FLUKA and MCNP simulations, and deal with the intensity and energy distribution of the neutron flux, the spatial profile of the neutron beam, the associated energy resolution and the beam related backgrounds. Several of these characteristics depend on the type of moderator and/or collimator used, and therefore all these cases have been discussed separately. Special attention has been given to estimate the systematic uncertainties of all these parameters, which are later propagated to estimate the overall uncertainty in the measurements performed at this facility.

Overall, the n\_TOF facility provides a very high instantaneous intensity ( $0.5\text{--}12 \times 10^6$  neutrons/pulse) beam of 3.5 or 10 cm and an excellent energy resolution in the complete energy interval of interest. Due to these characteristics, the n\_TOF facility stands today among the world leading facilities for measuring neutron-induced reactions.

Further information on the facility, the physics program and the experiments being carried out can be found on the official n\_TOF website <http://www.cern.ch/nTOF>.

The authors are indebted to the national and international funding agencies that have supported the n\_TOF Collaboration since its inception. In particular, this work was supported by the European Commission within the Fifth Framework Programme through nTOF-ND-ADS (contract no. FIKW-CT-2000-00107), the Sixth Framework Programme through EU-ROTRANS (FI6W-CT-2004-516520) and the Seventh Framework Programme through ERINDA (contract no. FP7-269499) and ANDES (contract no. FP7-249671). Furthermore, many measurements would not have been possible without the support from the CERN mechanical workshops (D. Grenier), the collaboration with JRC-IRMM through which most of the samples were obtained, the help and guidance of CERN/RP for the use of the radioactive samples, and the detectors fabricated at the CERN MicroMegas lab (R. de Oliveira, S. Ferry, A. Teixeira and A. Gris).

**Open Access** This is an open access article distributed under the terms of the Creative Commons Attribution License (<http://creativecommons.org/licenses/by/3.0>), which permits unrestricted use, distribution, and reproduction in any medium, provided the original work is properly cited.

## References

1. F. Käppeler, R. Gallino, S. Bisterzo, Wako Aoki, *Rev. Mod. Phys.* **83**, 157 (2011).
2. E. Fermi, L. Szilard, Neutronic Reactor, Patent number: 2708656, Filing date: Dec 19, 1944, Issue date: May 17, 1955.
3. IAEA: *International Status and Prospects of Nuclear Power*, <http://www.iaea.org/Publications/Booklets/NuclearPower/np08.pdf>.
4. *A Technology Roadmap for Generation IV Nuclear Energy Systems*, Issued by the U.S. DOE Nuclear Energy Research Advisory Committee and the Generation IV International Forum (December 2002).
5. W. Maschek, X. Chen, F. Delage, A. Fernandez-Carretero, D. Haas, C. Matzerath-Boccaccini, A. Rineiski, P. Smith, V. Sobolev, R. Thetford, J. Wallenius, *Prog. Nucl. Energy* **50**, 333 (2008).
6. The International Fusion Materials Irradiation Facility (IFMIF), <http://www.ifmif.org>.
7. IAEA Evaluated Nuclear Data Files, <http://www-nds.iaea.org/exfor/endl.htm>.
8. I. Dillmann, R. Plag, F. Käppeler, T. Rauscher, *KADoNiS v0.3 - The third update of the "Karlsruhe Astrophysical Database of Nucleosynthesis in Stars"*, <http://www.kadonis.org>.
9. The NEA Nuclear Data High Priority Request List (HPRL), [www.oecd-nea.org/dbdata/hprl](http://www.oecd-nea.org/dbdata/hprl).
10. R.A. Forrest, *Nuclear data for fusion applications*, in *Proceedings of the International Conference on Nuclear Data for Science and Technology 2007 (Nice, France)*, DOI: 10.1051/ndata:07713.
11. F. Gunsing *et al.*, *Nucl. Instrum. Methods B* **261**, 925 (2007).
12. N. Colonna, F. Belloni, E. Berthoumieux, M. Calviani, C. Domingo-Pardo, C. Guerrero, D. Karadimos, C. Lederer, C. Massimi, C. Paradela, R. Plag, J. Praena, R. Sarmiento, *Energy Environ. Sci.* **3**, 1910 (2010).
13. The n\_TOF Collaboration, *CERN n\_TOF Facility: Performance Report*, CERN/INTC-O-011, INTC-2002-037 CERN-SL-2002-053 ECT (2006).
14. E. Berthoumieux *et al.*, *The neutron Time-Of-Flight facility n\_TOF at CERN (I): Technical Description*, CERN n\_TOF Public Note n\_TOF-PUB-2013-001 (2013), [https://cds.cern.ch/record/1514680/files/n\\_TOF-PUB-2013-001.pdf](https://cds.cern.ch/record/1514680/files/n_TOF-PUB-2013-001.pdf).
15. M. Flaska, A. Borella, D. Lathouwers, L.C. Mihailescu, W. Mondelaers, A.J.M. Plompen, H. van Dam, T.H.J.J. van der Hagen, *Nucl. Instrum. Methods A* **531**, 392 (2004).
16. R. Reifarth, E.-I. Esch, A. Alpizar-Vicente, E.M. Bond, T.A. Bredeweg, S.E. Glover, U. Greife, R. Hatarik, R.C. Haight, A. Kronenberg, J.M. O'Donnell, R.S. Rundberg, J.M. Schwantes, J.L. Ullmann, D.J. Vieira, J.B. J.M. Wouters, *Nucl. Instrum. Methods B* **241**, 176 (2005).
17. K. Kino, M. Furusaka, F. Hiraga, T. Kamiyama, Y. Kiyonagi, K. Furutaka, S. Goko, H. Harada, M. Harada, T. Kai, A. Kimura, T. Kin, F. Kitatani, M. Koizumi, F. Maekawa, S. Meigo, S. Nakamura, M. Ooi, M. Ohta, M. Oshima *et al.*, *Nucl. Instrum. Methods A* **626-627**, 58 (2011).
18. E. Chiaveri *et al.*, Proposal for n\_TOF Experimental Area 2 (EAR-2), CERN-INTC-2012-029 / INTC-O-015.
19. The Frankfurt Neutron Source (FRANZ), <http://exp-astro.physik.uni-frankfurt.de/franz>.
20. C. Guerrero *et al.*, *Review of the n\_TOF experimental program for Reactor Applications*, to be published in EPJ Web of Conferences, Vol. **42** (2013).
21. The CERN Accelerator Complex, <http://public.web.cern.ch/public/en/research/AccelComplex-en.html>.
22. R. Plag *et al.*, *Nucl. Instrum. Methods A* **496**, 425 (2003).
23. C. Guerrero *et al.*, *Nucl. Instrum. Methods A* **608**, 424 (2009).
24. Y. Giomataris, Ph. Rebourgeard, J.P. Robert, G. Charpak, *Nucl. Instrum. Methods A* **376**, 29 (1996).
25. S. Andriamonje *et al.*, *J. Korean Phys. Soc.* **59**, 1597 (2011).
26. S. Marrone *et al.*, *Nucl. Instrum. Methods A* **517**, 389 (2004).
27. C. Weiss *et al.*, *PoS ENAS6*, 015 (2011).
28. C. Paradela *et al.*, *Phys. Rev. C* **82**, 034601 (2010).
29. U. Abbondanno *et al.*, *Nucl. Instrum. Methods A* **538**, 692 (2005).
30. The n\_TOF Collaboration (U. Abbondanno *et al.*), *Nucl. Instrum. Methods A* **521**, 454 (2004).
31. The n\_TOF Collaboration (G. Lorusso *et al.*), *Nucl. Instrum. Methods A* **532**, 622 (2004).
32. The n\_TOF Collaboration (C. Guerrero *et al.*), *Eur. Phys. J. A* **48**, 29 (2012).
33. G. Battistoni, S. Muraro, P.R. Sala, F. Cerutti, A. Ferrari, S. Roesler, A. Fassò, J. Ranft, *AIP Conf. Proc.* **896**, 31 (2006).
34. A. Fassò, A. Ferrari, J. Ranft, P.R. Sala, *Fluka: A multi-particle transport code*, Technical Report CERN-2005-10, INFN/TC.05/11, SLAC-R-73 (2005).
35. L.S. Waters, G.W. McKinney, J.W. Durkee, M.L. Fensin, J.S. Hendricks, M.R. James, R.C. Johns, D.B. Pelowitz, *AIP Conf. Proc.* **896**, 81 (2007).
36. V. Vlachoudis, *FLAIR: A powerful but user friendly graphical interface for FLUKA*, in *Proceedings of the International Conference on Mathematics, Computational Methods and Reactor Physics, Saratoga Springs, New York, 2009*, <http://www.fluka.org/flair/Flair-MC2009.pdf>.

37. R. Macklin, J. Halperin, R. Winters, Nucl. Instrum. Methods A **164**, 213 (1979).
38. A.D. Carlson, V.G. Pronyaev, D.L. Smith, N.M. Larson, C. Zhenpeng, G.M. Hale, F.J. Hamsch, E.V. Gai, Soo-Youl Oh, S.A. Badikov, T. Kawano, H.M. Hofmann, H. Vonach, S. Tagesen, Nucl. Data Sheets **110**, 3215 (2009).
39. The n\_TOF Collaboration (M. Barbagallo, N. Colonna, C. Guerrero, A. Tsignais), in preparation.
40. D.B. Gayther, Metrologia **27**, 221 (1990).
41. C. Guerrero *et al.*,  $^{241}\text{Am}$  neutron capture measurements at n\_TOF, in *Proceedings of the Final Scientific EFNUDAT Workshop*, ISBN: 978-92-9083-365-9, <http://indico.cern.ch/getFile.py/access?resId=0&materialId=1&confId=83067>.
42. K. Fraval *et al.*, *Analysis of  $^{241}\text{Am}(n,\gamma)$  cross section with  $\text{C}_6\text{D}_6$  detectors*, to be published in Nucl. Data Sheets.
43. J. Pancin *et al.*, Nucl. Instrum. Methods A **524**, 102 (2004).
44. F. Belloni *et al.*, Phys. Scr. **2012**, 014004 (2012).
45. N. Larson, *Updated Users' Guide for SAMMY: Multi-level R-Matrix fits to neutron data using Bayes' equations*, ORNL/TM-9179/R8 ENDF-364/R2 (October 2006).
46. M.C. Moxon, T.C. Ware, C.J. Dean, *REFIT-2009 A Least-Square Fitting Program for Resonance Analysis of Neutron Transmission, Capture, Fission and Scattering Data*, Users' Guide for REFIT-2009-10 (UKNSF(2010)P243, April 2010).
47. C. Coceva *et al.*, Nucl. Instrum. Methods A **489**, 2002 (346).
48. F. Gunsing *et al.*, Phys. Rev. C **85**, 064601 (2012).
49. The Joint Evaluated Fission and Fusion File (JEFF-3.1.2) [http://www.oecd-nea.org/dbforms/data/eva/evatapes/jeff\\_31/JEFF312/](http://www.oecd-nea.org/dbforms/data/eva/evatapes/jeff_31/JEFF312/).
50. G. Tagliente *et al.*, Phys. Rev. C **77**, 035802 (2008).
51. C. Lederer *et al.*, Phys. Rev. C **83**, 034608 (2011).
52. T. Wright *et al.*, *High-precision measurement of the  $^{238}\text{U}(n,\gamma)$  cross section at n\_TOF CERN*, to be published in Nucl. Data Sheets.